ACS APPLIED ENERGY MATERIALS

www.acsaem.org

Forum Article

Two-Dimensional Double Perovskites in the Dion–Jacobson Phase Alleviate Parity Forbidden Transitions for Photovoltaic Applications

Robert Stanton and Dhara J. Trivedi*

Cite This: https://doi.org/10.1021/acsaem.3c03276

Read Online

ACCESS | Metrics & More | Article Recommendations | Supporting Information

ABSTRACT: Two-dimensional double perovskites have recently been identified as a potential class of materials for the improvement of halide-perovskite-based solar cell technology. The expanded set of utilizable B- and B′-site cations afforded to double perovskites, combined with tunable structural and electronic properties in two-dimensional perovskites, leads to a highly modifiable set of materials, which have yet to be explored. In this study, we investigate the structural, electronic, and thermoelectric properties of these materials and identify a number of key structure–property relationships governing their performance. In the process, we demonstrate a link between the relative electronegativities of the building components and the resultant geometric structures. Furthermore, we provide insights aimed toward alleviating concerns associated with parity forbidden transitions which plague many double perovskite systems. In addition, we identify a number of two-dimensional double perovskites including the mixed-oxidation state $In_{25}Tl_{75}Cl$-based system which displays optically active transitions as low as 1.41 eV across the Brillouin zone and indicators pointing toward stable experimental synthesis.

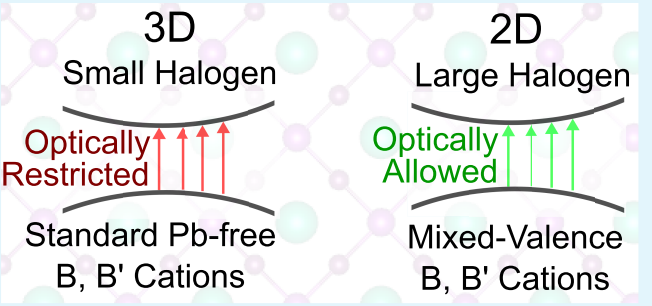

KEYWORDS: *double perovskites, two-dimensional materials, photovoltaics, thermoelectric, solar energy harvesting, absorption*

INTRODUCTION

Perovskite-based photovoltaics have served as an indispensable class of materials in solar energy harvesting for decades, with improvements over the past decade leading to power conversion efficiencies as high as 25.8%.[1−3] Perovskite solar cells, however, exhibit persistent challenges regarding stability, toxicity of building components, and device longevity which motivate ongoing research efforts to mitigate these pitfalls.[4−8] These efforts can largely be categorized by one of three approaches: (1) the investigation into perovskite-based materials of reduced dimensionality, most commonly two-dimensional perovskites (2DPKs), (2) the utilization of a singular replacement divalent B-site cation such as tin or germanium, or (3) the employment of lead-free mixed-metal perovskites that have been termed double perovskites (DPKs) in the literature.[9−16] The above approaches have broadly expanded the search space of perovskite-based photovoltaic materials, and mixed success has been achieved in identifying materials which maintain the optoelectronic properties that make lead-iodide perovskites so attractive while mitigating the concerns that come along with them.[17−19]

Bulk perovskites exhibit a chemical formula of ABX_3, with the most typical A/B charge ratio being 1:2 for photovoltaic applications. The additional complexity of double perovskites comes in the form of allowing for combinations of monovalent and trivalent metals at the B-site, which results in a chemical formula of $A_2BB'X_6$.[11,20,21] While mixed-divalent cations at the B-, B′-sites are also possible, these are not as well-explored as the B^{I}, B'^{III} double perovskites in the literature. In terms of perovskites of reduced dimensionality, the family of 2DPKs come in several phases, the two most common of which are the Ruddlesden–Popper (RP) and Dion–Jacobson (DJ) phases.[22] These respectively have chemical formulas of $A'_2A_{n-1}B_nX3_{n+1}$ and $A'A_{n-1}B_nX3_{n+1}$, where the A′ cation represents a long organic molecule which spatially separates adjacent perovskite layers, and n represents the number of inorganic octahedra in each two-dimensional layer of the material. The difference in stoichiometry of the A′ cation between the RP and DJ phase comes from the fact that in the DJ phase, the spacer molecule is typically shared between adjacent inorganic layers, resulting in a 1+ (2+) A′ cation in the RP (DJ) phase.

The introduction of these new approaches to generate highly performant photovoltaic perovskites naturally comes with its own sets of challenges. DPKs have been established to display parity-forbidden transitions in a number of materials which would otherwise serve as highly desirable photovoltaics.[23−25] 2DPKs, on the other hand, struggle with wider bandgaps when

Special Issue: Early Career Forum 2024

Received: December 30, 2023
Revised: February 25, 2024
Accepted: March 21, 2024

Table 1. Structural Properties Associated with the 18 2DDPKs Used in the Present Study

2DDPK	Σ (deg)	Δ	Λ_2 (Å^2)	t_g	μ	X_{BX}	B-X_{ave} (Å)	E_{form} (eV)
AuBiCl	10.93	2.8×10^{-2}	1.9×10^{-01}	0.87	0.66	0.88	3.04	−3.78
AuBiI	11.14	2.3×10^{-2}	2.0×10^{-01}	0.85	0.55	0.38	3.34	−3.57
AuSbCl	11.33	3.0×10^{-2}	3.0×10^{-01}	0.91	0.59	0.87	3.02	−3.77
AuSbI	10.89	2.5×10^{-2}	7.0×10^{-01}	0.88	0.48	0.37	3.34	−3.57
$In_{25}Tl_{75}Cl$	4.87	1.6×10^{-3}	8.9×10^{-02}	0.88	0.64	1.50	2.86	−3.78
$In_{25}Tl_{75}I$	3.46	6.9×10^{-4}	6.7×10^{-02}	0.86	0.53	1.00	3.17	−3.56
$In_{75}Tl_{25}Cl$	4.83	2.0×10^{-3}	7.3×10^{-02}	0.83	0.73	1.42	2.86	−3.81
$In_{75}Tl_{25}I$	3.56	2.7×10^{-4}	7.5×10^{-02}	0.82	0.60	0.92	3.16	−3.59
InBiCl	4.66	4.6×10^{-4}	9.5×10^{-02}	0.87	0.66	1.26	2.90	−3.80
InBiI	3.26	2.9×10^{-4}	4.9×10^{-02}	0.85	0.54	0.76	3.18	−3.59
InSbCl	4.75	1.7×10^{-3}	7.7×10^{-02}	0.91	0.58	1.25	2.88	−3.79
InSbI	3.04	3.4×10^{-4}	4.7×10^{-02}	0.89	0.48	0.75	3.15	−3.58
InTlCl	4.08	4.5×10^{-4}	3.9×10^{-02}	0.89	0.62	1.46	2.85	−3.81
InTlI	3.59	3.6×10^{-4}	8.1×10^{-02}	0.87	0.51	0.96	3.16	−3.58
TlBiCl	5.06	5.8×10^{-4}	9.3×10^{-02}	0.85	0.70	1.34	2.94	−3.80
TlBiI	4.15	4.0×10^{-4}	1.1×10^{-01}	0.83	0.58	0.84	3.23	−3.59
TlSbCl	5.11	1.0×10^{-3}	8.6×10^{-02}	0.89	0.62	1.33	2.90	−3.79
TlSbI	3.86	4.2×10^{-4}	8.5×10^{-02}	0.87	0.51	0.83	3.19	−3.58

compared with their bulk counterparts, particularly when the layer thickness, n, is on the order of 1−5.[26] Combinations of double perovskites and two-dimensional perovskites, herein referred to as 2DDPKs, have only emerged very recently in the literature.[27−30] The introduction of 2DDPKs allows for many combinations of monovalent and trivalent cations to mitigate the wide bandgap concerns of 2DPKs, as well as selection of the A′ spacing cations to reduce symmetry and alleviate the otherwise forbidden optical transitions at the band edge. While the potential of 2DDPKs is very promising, limited research has been carried out on a subset of these materials simultaneously to aid in generalizing the key structure−property relationships in this subclass of perovskites.[31] To address this gap in the literature, in this work, we use *ab initio* density functional theory (DFT) calculations to consider 18 n = 2 2DDPKs in the DJ phase all employing A′ = 3-(aminomethyl)piperidinium (3AMP), and A = cesium (Cs). We investigate the structural, electronic, and thermoelectric properties of these materials and uncover the importance of elemental electronegativities for the resulting 2DDPK geometry, key insights toward alleviating concerns associated with parity forbidden transitions, and an excellent linearly scaling relationship between PBE band gaps and those which can be directly compared with the experiment by way of the GLLB-sc functional.[32] Furthermore, we identify a number of new 2DDPKs including the novel mixed-oxidation state $In_{25}Tl_{75}Cl$-based 2DDPK, which displays optically active transitions as low as 1.41 eV across the Brillouin zone (BZ) and indicators pointing toward stable experimental synthesis.

RESULTS AND DISCUSSION

We constructed initial structures of all 2DDPKs using the Pyrovskite package, allowing for the uniform generation of 2DDPKs with varied building components.[33] We employed combinations of monovalent metals at the B-site of M^{I} = Au, In, Tl, trivalent metals at the B′-site of M^{III} = Bi, Sb, Tl, and halogens at the X-site of X = Cl, I. This selection comprises both novel B-, B'-site combinations as well as some known to exhibit band gaps in the bulk phase which are favorable to photovoltaic applications such as In, Sb.[34−36] Our selection here was informed by previous work carried out by Meng et al. concerning the optical availability associated with different B-, B′-site pairings in bulk double perovskites.[23] Noted in their work are the large optical issues associated with monovalent B-site cations such as Na, K, Rb, Cs, Ag, Au, and Cu. With this being the case, we focus primarily on the more favorable In- and Tl B-site cations, with the inclusion of Au to assess the extension of their work to double perovskites. Due to the fact that all 2DDPKs in the present study contain A′ = 3AMP, and A = Cs, in discussion we identify the perovskite by the B, B′, and X building components, such as InSbI. We also exploited the fact that both In, and Tl can exhibit 1+ and 3+ oxidation states, to consider 0.25 and 0.75 occupancies of these cations, herein referred to as $In_{25}Tl_{75}X$ and $In_{75}Tl_{25}X$, respectively.[37] The full list of structures and associated geometric properties can be found in Table 1. We found all structures except those containing Au at the B-site to crystallize in stable perovskite structures with intact octahedra upon density functional theory (DFT) geometry optimization. In all four Au-containing 2DDPKs, the Au-X interactions result in the formation of AuX_2 fragments which do not generate a stable perovskite structure. We've computed octahedral distortion parameters Σ, which represents the deviation from idealized X-B-X bond angles in the BX_6 octahedra; Δ, which represents deviations from average B-X bond lengths; and Λ_2, which describes diagonal dislocations of the B-cation within the planes of the octahedra. X_{BX} in Table 1 represents a weighted absolute difference between the Pauling electronegativities of the B, B′ site cations and the X halogens, as detailed in eq 1 below where w_B and $w_{B'}$ correspond to the stoichiometric weightings of the B-, B′-sites cations, and X_i corresponds to the Pauling electronegativity of element i.

$$X_{BX} = \left| \frac{w_B X_B + w_{B'} X_{B'}}{2} - X_X \right| \quad (1)$$

We computed Pearson correlation coefficients between X_{BX} and the octahedral distortion parameters across the 18 2DDPKs and note a strong negative correlation between these octahedral distortion parameters and X_{BX}, ranging from −0.48 to −0.57. This implies that the large electronegativity difference between B, B′, and X components confers a rigidity to the resultant perovskite which we rationalize by the

https://doi.org/10.1021/acsaem.3c03276
ACS Appl. Energy Mater. XXXX, XXX, XXX−XXX

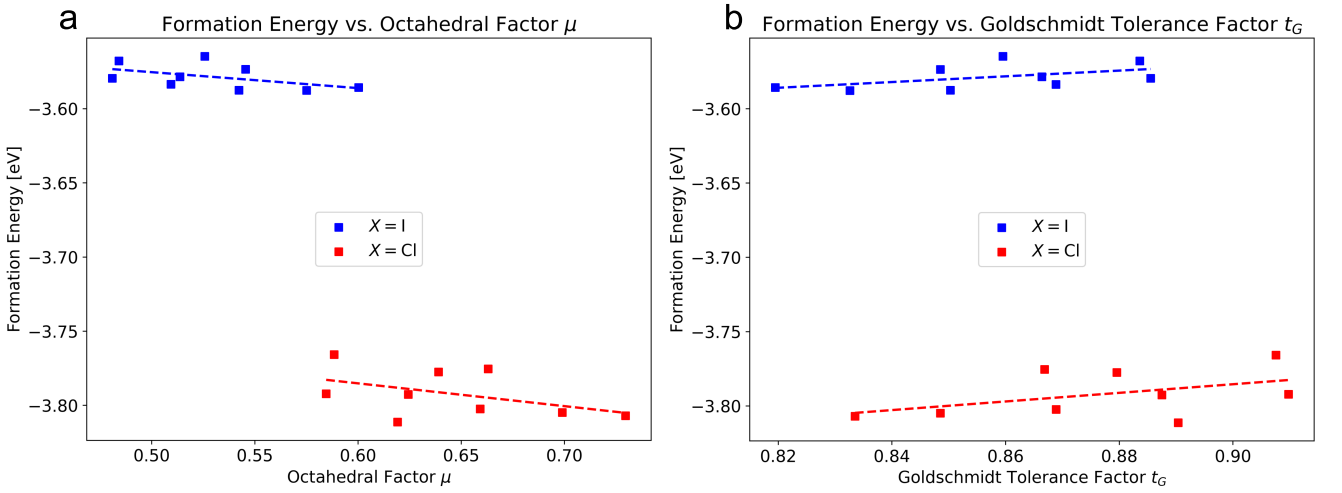

Figure 1. (a) Formation energy vs octahedral factor μ and (b) formation energy vs Goldschmidt tolerance factor t_G for the 18 2DDPKs in the present study. Dashed lines represent linear fits for each subset of X-halogens.

increased ionic nature of B-X and B′-X interactions, producing closer to idealized octahedral structure. This provides valuable insight for scenarios where distortions in perovskite octahedra are necessary to facilitate the tuning of band gaps, or to increase the optical availability of low energy transitions by reducing or removing symmetries present. Additionally, average B-X, B′-X bond distances (B-X_{ave} in Table 1) are reduced in the Cl-containing perovskites compared with the corresponding I-containing systems by 0.295 Å, resulting in smaller in-plane lattice parameters as well as increased stability as indicated by formation energies which experience a commensurate decrease of on average 0.21 eV. This is largely attributed to the smaller ionic radius of the chloride ion compared to that of iodide.[38]

The Goldschmidt tolerance factor (t_G) and octahedral factor (μ) are two parameters computed from the ionic radii of the A-, B-, and X-site ions in bulk perovskites as a heuristic to indicate the stability and phase of the perovskite once synthesized.[39,40] We adapt these formulas to use a weighting of the B- and B′-site ions to compute an average ionic radius $\tilde{R}_B$ for usage in DPKs as detailed in eqs 2, 3, and 4. In eq 2, w_i^I and denote the stoichiometric weighting necessary to obtain the weighted average of ionic radii, and $R_{B_i^I}$ denotes the ionic radius of element i in oxidation state I obtained from Shannon et al.[38]

$$\tilde{R}_B = \sum_{B_i^I} w_i^I R_{B_i^I} \tag{2}$$

$$t_G = \frac{(R_A + R_X)}{\sqrt{2}^*(\tilde{R}_B + R_X)} \tag{3}$$

$$\mu = \frac{\tilde{R}_B}{R_X} \tag{4}$$

Regions of stability for the tolerance factors in bulk DPKs are $0.813 < t_G < 1.107$, and $0.377 < \mu < 0.895$ respectively.[41] The dimensional reduction to 2DPKs, especially for low layer thicknesses, n, can in some cases expand the acceptable t_G and μ ranges. This is largely because corrugation in the out-of-plane direction can alleviate the geometric issues associated with mismatched ionic radii.[38] Figure 1 shows the formation energies plotted against t_G and μ for all 18 2DDPKs in the present study. Formation energies are computed as shown in eq 5, where E_{2DDPK} is the DFT energy of the full 2DDPK system, N_i represents the number of atoms in the unit cell of element i, and E_i represents the DFT energy of the lone element i. With this formulation, a lower E_{form} corresponds to an increasingly stable atomic configuration compared with the constituent atoms in the system.

$$E_{form} = E_{2DDPK} - \sum_i N_i E_i \tag{5}$$

We observe a trend toward energetic preference of larger values of μ in the 2DDPKs shown here which is consistent with the orthorhombic phases obtained upon DFT optimization.[41] It is important to note that the 2DDPKs consistently showed improved formation energies approaching the lower bound of what are considered acceptable t_G values in bulk perovskites. For reference t_G of the ubiquitous $MAPbI_3$ perovskite is 0.81, and our results suggest that 2DDPKs may be feasible to synthesize at or beyond this boundary.[42] Thus, our results show that the search space of potentially stable 2DDPKs may include B, B′ cations of larger ionic radii than would otherwise be tolerable in bulk DPKs. Furthermore, this indicates that setting hard boundaries comparable to those used in the high-throughput screening of bulk perovskites should not be done so rigidly in future investigations of 2DDPKs. In fact, this remains true when considering not only the structural but also the optoelectronic properties of these 2DDPK systems.

Optoelectronic properties are the key determining factors for the photovoltaic performance of a given set of materials. With this being the case, we carried out an extensive investigation of the electronic structure present in the 18 2DDPK systems used in the present study. We computed electronic band structures with and without spin−orbit coupling (SOC) at the DFT+PBE level. Additionally, because both DFT-level and DFT+SOC-level calculations tend to severely underestimate electronic bandgaps, for all systems gapped at the PBE level we compute the GLLB-sc band gap, which has been demonstrated to provide excellent agreement with experiment.[43] The GLLB-sc approach serves as a

https://doi.org/10.1021/acsaem.3c03276
ACS Appl. Energy Mater. XXXX, XXX, XXX−XXX

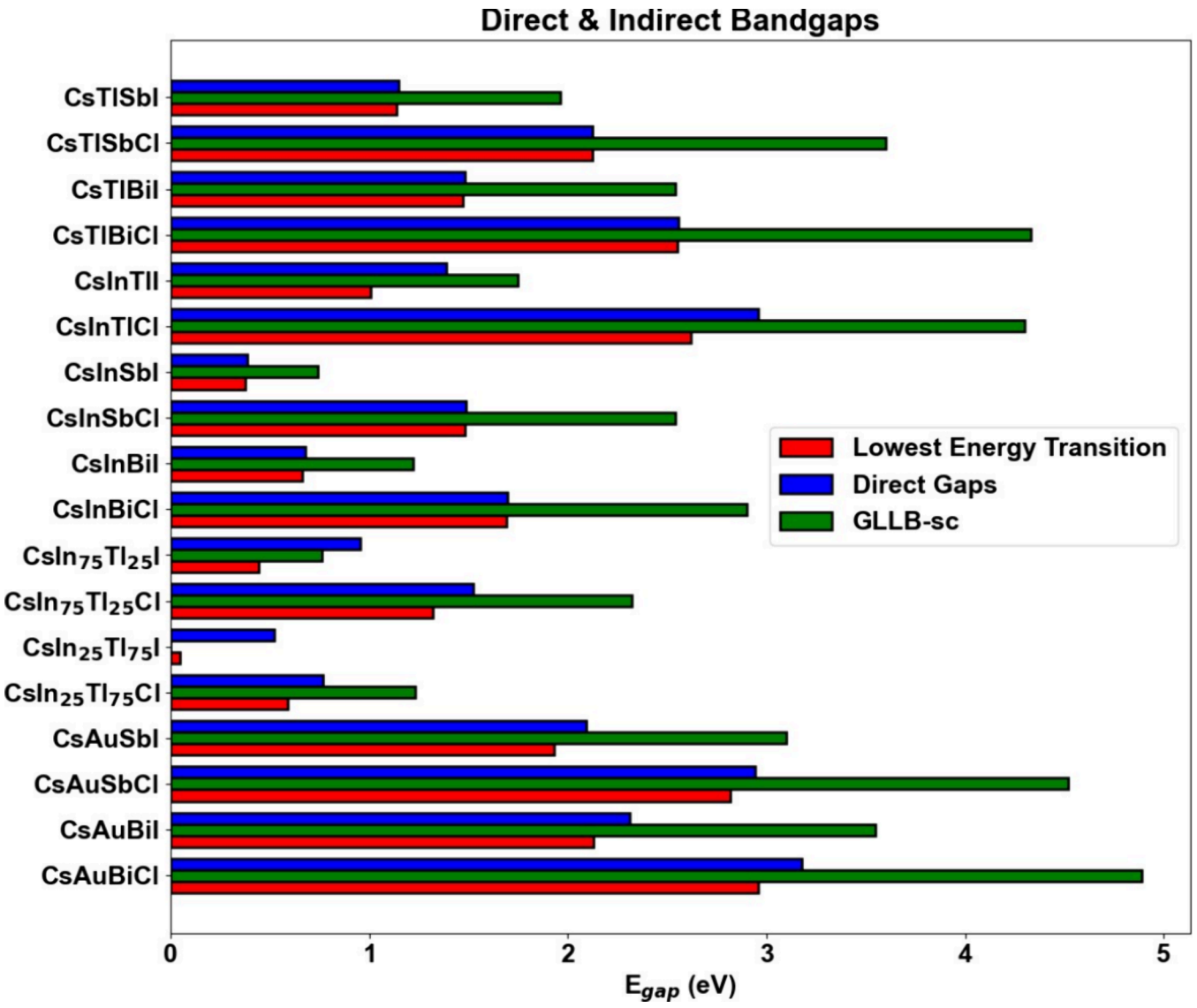

Figure 2. Electronic bandgaps computed at the PBE, and GLLB-sc level for all 18 2DDPKs used in the present study. Lowest energy transitions and direct band gaps correspond to the directly gapped 2DDPKs.

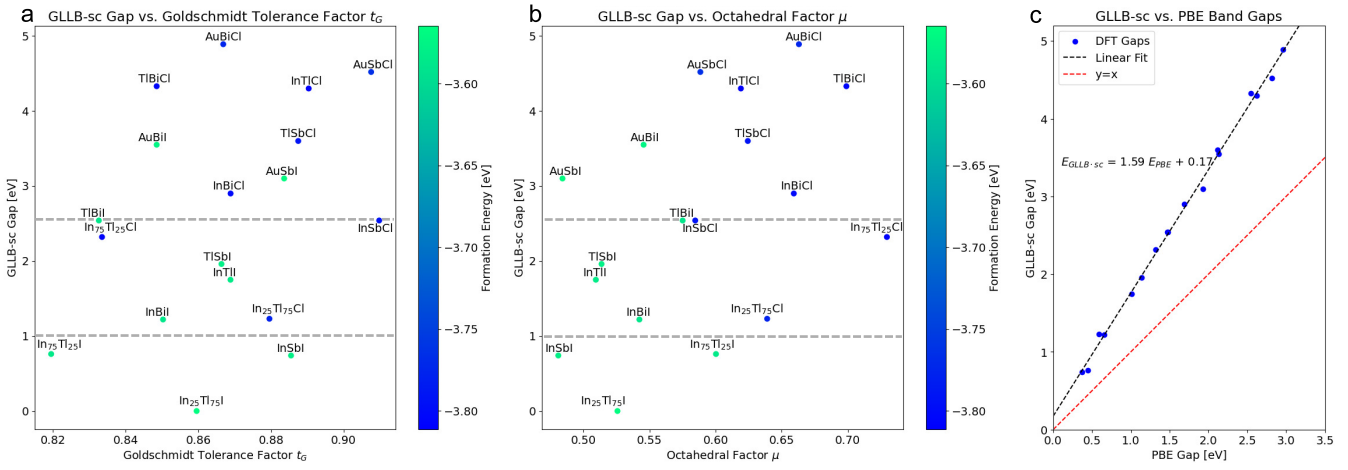

Figure 3. GLLB-sc gaps vs (a) Goldschmidt tolerance factor t_G, and (b) octahedral factor μ for the 18 2DDPK systems used in the present study. Points are colored by the formation energies. The regions enclosed by dashed lines represent systems exhibiting band gaps between 1.0 and 2.5 eV. (c) GLLB-sc gaps compared with PBE gaps from DFT computed band structures with the linear scaling relationship in the inset.

https://doi.org/10.1021/acsaem.3c03276
ACS Appl. Energy Mater. XXXX, XXX, XXX−XXX

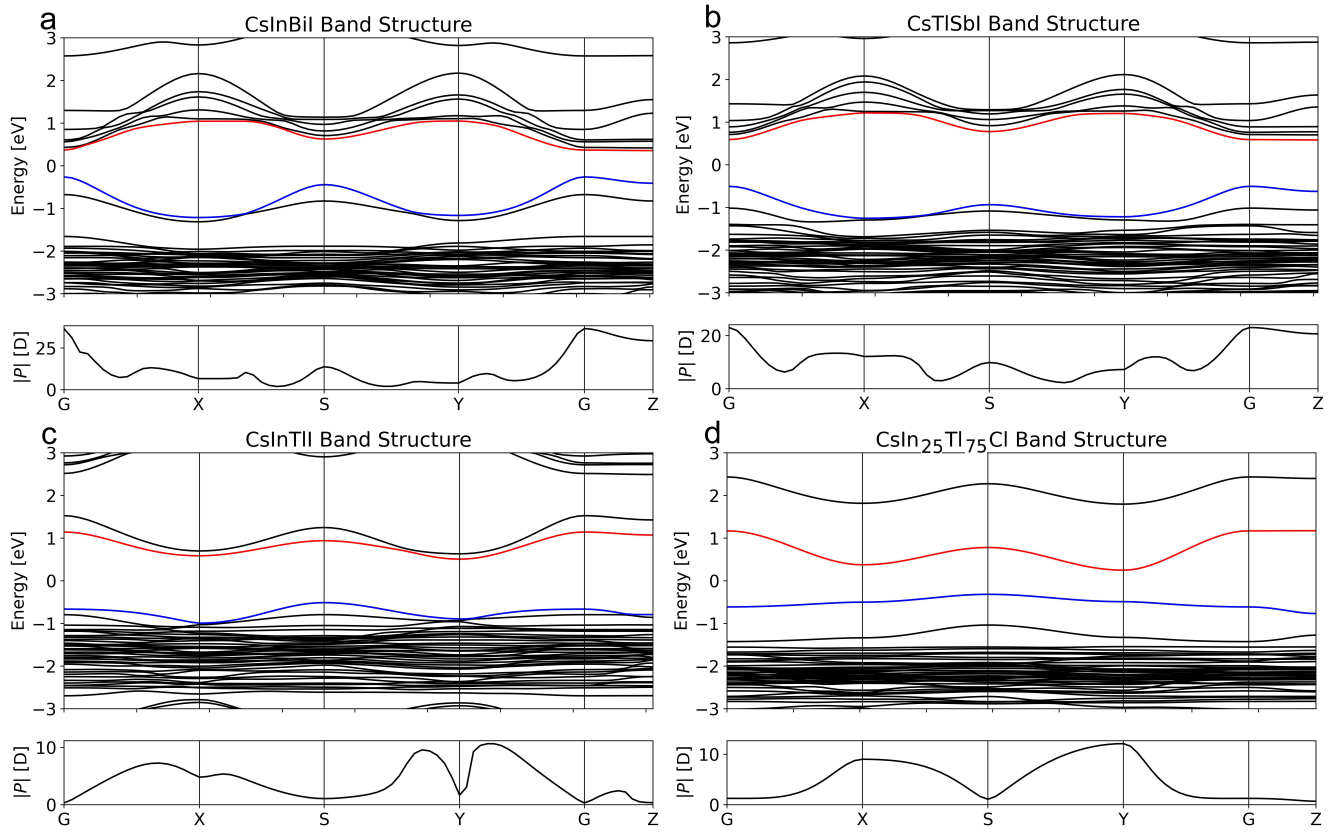

Figure 4. Band structures of the (a) InBiI, (b) TlSbI, (c) InTlI, and (d) $In_{25}Tl_{75}Cl$ perovskites. Transition dipole moments across the high symmetry paths are presented below each respective band structure and were computed for direct transitions between the VBM (blue) and CBM (red).

correction to typical DFT band gaps, whereby the underestimation is mitigated by a correction associated with the derivative discontinuity in the system of interest. This approach has been benchmarked across a wide array of semiconductor systems, including hybrid double perovskites, consistently outperforming even approaches using hybrid functionals like HSE06.[43,44] Figure 2 displays electronic band gaps associated with direct and indirect (where applicable) DFT+PBE level results, as well as the GLLB-sc level results computed for more direct correspondence with expected experimental values. As noted by Zhan et al. desirable photovoltaic materials in the subclass of perovskites have experimental band gaps of approximately 1−2.5 eV, with the ideal band gap as dictated by the Shockley-Queisser limit of 1.34 eV.[41] Figure 3a, b displays the GLLB-sc band gaps against both t_G and μ, with the dashed region representing the 2DDPKs with band gaps within this desirable region. We largely see that the Au-containing 2DDPKs exhibit band gaps well outside of this range, making them undesirable for usage in photovoltaic solar cells, even if the previously mentioned structural instability indicators could be remedied. Furthermore, the interchange of X-site halogen from chloride to iodide leads to a relatively uniform decrease in band gap of on average 1.68 eV, with a standard deviation of 0.36 eV. An additional insight is the very linear relationship between DFT gaps computed at the PBE level and at the GLLB-sc level (Figure 3c). Simple linear regression suggests an effective and accurate means for approximating band gaps at the GLLB-sc level from a simple PBE calculation detailed in eq 6.

$$\tilde{E}_{\mathrm{GLLB-sc}} = 1.59E_{\mathrm{PBE}} + 0.17 \quad (6)$$

Here $\tilde{E}_{\mathrm{GLLB-sc}}$ is the zero-cost approximation to the GLLB-sc gap which can be obtained from directly from the band gap at the PBE level, E_{PBE}. Information of this nature can greatly aid in future computational workflows that aim to mitigate computational cost by forecasting band gaps for closely related perovskite systems of interest. The large energy range of accuracy observed from this extrapolation technique (Figure 3c) suggests its applicability to similar 2DPKs and 2DDPKs which may be the focus of future investigations. We would, however, caution the usage of this extrapolation technique to perovskite systems that differ significantly in their chemical composition, such as perovskite oxides or perovskites including lanthanides or actinides as B-site cations. The dashed regions of Figure 3a, b display a number of 2DDPK systems that are candidates for photovoltaic applications, the four of which that are closest to the idealized gap of 1.34 eV while remaining between 1.0 and 2.5 eV are TlSbI, InTlI, InBiI, and the novel mixed oxidation state $In_{25}Tl_{75}Cl$ systems. We also note that the InSbI, and $In_{75}Tl_{25}I$ systems, while having band gaps slightly below 1.0 eV, may also serve as effective materials in photovoltaic applications. Previously Zhang et al. have investigated a bulk analog to the InSbI system with X = Cl and found it to have optically active transitions at the band edge and a desirable band gap, in congruence with our results (Figure S12), albeit with notable structural instabilities.[34]

As previously mentioned, a key concern in the usage of DPKs is the presence of optically inactive transitions, which

https://doi.org/10.1021/acsaem.3c03276
ACS Appl. Energy Mater. XXXX, XXX, XXX−XXX

Table 2. Thermoelectric Properties of the 2DDPKs Used in the Present Study[a]

2DDPK	E_{VBM} (eV)	E_{CBM} (eV)	C^{2D} (Nm^{-1})	m_h^*	m_e^*	τ_h (fs)	τ_e (fs)	TPF_{300h} ($mW\ K^{-2}\ m^{-1}$)	TPF_{800e} ($mW\ K^{-2}\ m^{-1}$)	TPF_{300e} ($mW\ K^{-2}\ m^{-1}$)	TPF_{800e} ($mW^{-2}\ m^{-1}$)
AuBiCl	8.83	6.68	32.50	1.18	1.96	3.00	2.86	0.08	0.08	0.09	0.08
AuBiI	9.51	6.43	37.20	1.76	1.98	3.67	1.88	0.09	0.09	0.11	0.15
AuSbCl	8.67	6.25	31.74	1.31	1.60	4.10	2.61	0.08	0.06	0.09	0.08
AuSbI	9.10	6.52	32.44	1.86	1.60	3.85	1.70	0.09	0.06	0.08	0.09
$In_{25}Tl_{75}Cl$	10.47	7.33	46.66	1.30	0.39	17.74	2.65	0.47	0.27	0.14	0.24
$In_{75}Tl_{25}Cl$	11.51	6.89	48.50	1.08	0.46	18.08	2.73	0.54	0.56	0.14	0.22
$In_{75}Tl_{25}I$	11.63	7.30	38.32	0.40	0.50	11.67	5.77	0.57	0.39	0.27	0.31
InBiCl	12.06	7.33	44.88	0.14	0.36	18.79	17.80	0.97	1.63	0.99	1.92
InBiI	11.39	8.03	40.80	0.04	0.06	83.62	57.55	3.71	10.16	3.48	9.11
InSbCl	11.05	6.41	40.32	0.27	0.33	23.69	9.75	1.23	2.16	0.54	1.05
InSbI	11.16	8.00	40.27	0.05	0.07	68.99	49.02	2.78	7.39	4.01	8.04
InTlCl	10.50	7.16	43.32	0.69	0.54	12.52	4.57	0.42	0.46	0.24	0.40
InTlI	10.32	7.74	30.65	0.96	0.51	8.08	2.42	0.34	0.40	0.12	0.23
TlBiCl	10.67	7.02	40.03	0.19	0.43	15.36	15.27	0.75	1.16	0.82	1.52
TlBiI	10.54	8.24	38.40	0.12	0.14	31.82	22.41	1.49	2.69	1.81	3.77
TlSbCl	9.97	7.06	39.65	0.41	0.46	13.99	7.78	0.66	1.08	1.39	2.62
TlSbI	10.55	8.12	38.90	0.11	0.14	35.18	26.23	1.64	3.15	2.33	4.87

[a]The gapless $In_{25}Tl_{75}I$ perovskite is omitted from these results due to its lack of band gap at the PBE level.

render an otherwise desirable photovoltaic material ineffective for solar energy harvesting. With this being the case, for all perovskites, we compute the transition dipole moments (TDMs) between the valence band maxima (VBM) and conduction band minima (CBM) across the high symmetry paths used for computation of the DFT band structures. Figure 4 shows band structures and TDMs between the VBM and CBM for the four candidate materials identified above as promising photovoltaics. The band structures, TDMs and density of states (DOS) for all perovskites are also available in the Supporting Information (Figures S3−S29). From Figure 4, we see that both InBiI and TlSbI are directly gapped at the Γ-point, with TDMs of over 20 D between the band edges and GLLB-sc gaps of 1.22 and 1.95 eV respectively. In the case of InBiI, transitions at the band edge correspond to primarily I(p) and In(s) states at the VBM, and Bi(p), I(p), and In(p) states at the CBM. Similarly, in the TlSbI 2DDPK, the VBM consists of I(p) states and the CBM is constituted by Sb(p), Tl(p), and I(p) states. Tabular information about whether the system is directly or indirectly gapped, the primary subshells contributing to the band edges, the PBE as well as GLLB-sc band gaps, and the optical availability of low energy transitions can be found in Table S1. The InTlI and $In_{25}Tl_{75}Cl$ 2DDPKs are both indirectly gapped with GLLB-sc gaps of 1.75 and 1.23 eV, respectively, which correspond to 2.13 and 1.41 eV for the corresponding direct transitions. Both structures contain large portions of the band paths, which are optically active near these lowest energy direct transitions. In particular, the $In_{25}Tl_{75}Cl$ presents itself as a key candidate photovoltaic material with optically active transitions in key parts of the BZ. Moving from S-X and Y-X, optical gaps narrow and TDMs increase to approximately 10 D. This fact combined with its direct gap of 1.41 eV makes this a very promising candidate 2DDPK.

Further investigating the novel mixed-valence $In_{25}Tl_{75}Cl$ system, we note that the wide availability of low energy transitions from the X−S-Y path contrasts with the case of InBiI and TlSbI, whereby band gaps widen significantly across the BZ when moving away from the Γ and S points. Additionally, we compute Bader charges to quantify how charge distributes across the mixed-valence sites, and find partial atomic charges of $q_{In} = +1.59$ for the lone indium in the unit cell, and $q_{Tl} = +0.74$, + 0.71, and +1.23. This indicates a clear retention of the mixed oxidation states of the three thallium atoms in the unit cell. We found that symmetry breaking associated with introducing mixed stoichiometries can aid in reducing the prevalence of parity forbidden transitions in this class of materials. The $In_{25}Tl_{75}Cl$ system contains band edges consisting of Cl(p) and In(s,p) contributions near the VBM and In(s,p), Cl(p) bands near the CBM. Typically, metal-to-metal transitions of similar character are those which exhibit the parity forbidden transitions in DPKs, attributable to the symmetry of the corresponding orbitals. Our results, however, suggest that considering mixed oxidation states can drastically modify the shapes of these orbitals (Figure S30), and result in over a 2-fold increase in TDMs when comparing the mixed oxidation state $In_{25}Tl_{75}Cl$ system to that of the InTlCl system. In fact, a similar increase in TDMs by way of antimony doping in the $Cs_2AgIn_{0.75}Sb_{0.25}Cl_6$ bulk DPK was observed by Zhang et al. supporting this conclusion.[34] As a final note on the remediation of parity forbidden transitions in 2DDPKs, we uncovered a consistent two- to 4-fold increase in TDMs (Figures S3, S6, S9, S12, S15, S18, S21, S24, and S27) for all I-containing systems when compared with their Cl-containing counterparts. This appears to be attributable to the large ionic radius of iodide (2.2 Å) compared with that of the chloride ion (1.81 Å), inducing greater mixing of states compared to the high-symmetry lone atomic orbitals. This is further supported by the modulation of TDMs upon band crossing between B-, or B′-site cations and I-anions. An illustrative example of this can be seen in the InTlI perovskite (Figure S27) whereby a band crossing along the S−Y path drastically increases the magnitude of the TDMs when the I-band is found to be lower in energy than the Tl-band.

To broaden the scope of applicability for perovskite based solar energy harvesters, much research in the literature has been put forth to investigate their usage in hybrid photovoltaic-thermoelectric (PV-TE) devices. With this being the case, we have used a two-step approach of pairing DFT-based

https://doi.org/10.1021/acsaem.3c03276
ACS Appl. Energy Mater. XXXX, XXX, XXX−XXX

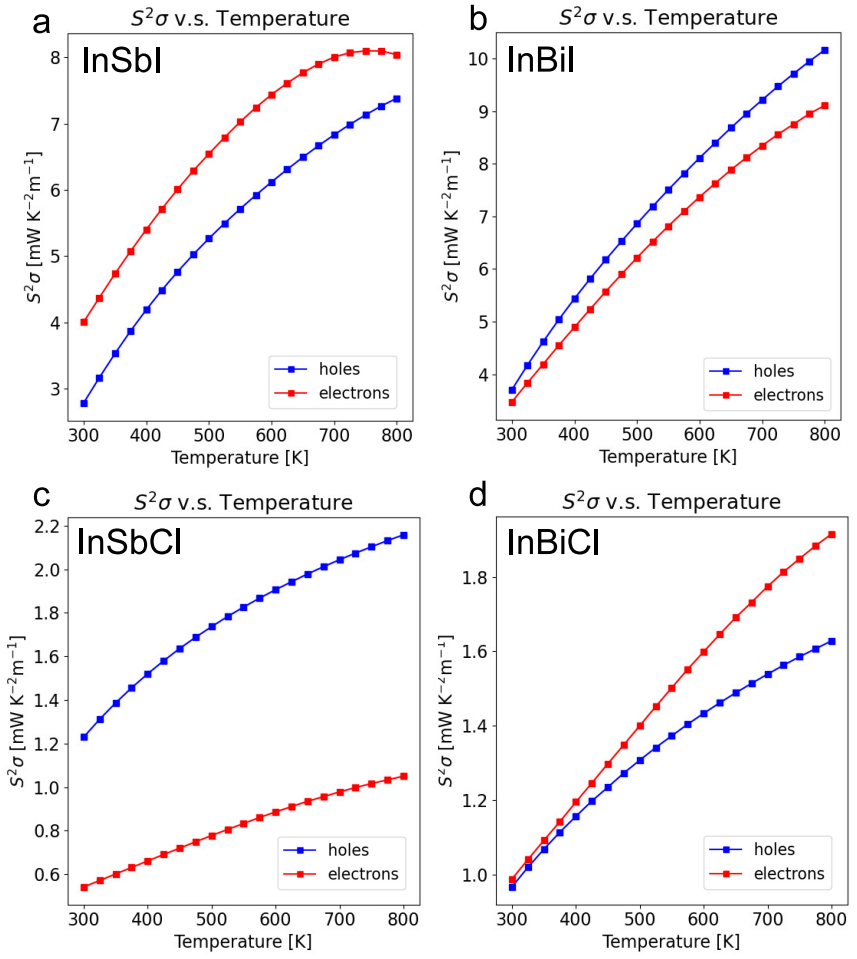

Figure 5. Thermoelectric power factor of the n-doped and p-doped configurations of the (a) InSbI, (b) InBiI, (c) InSbCl, and (d) InBiCl 2DDPKs from 300 to 800 K.

deformation potential theory with solution of the Boltzmann Transport Equations (BTEs) to assess the thermoelectric performance of these 2DDPKs under a broad range of conditions. All BTE calculations are carried out in the relaxation time approximation as implemented in BoltzTraP2.[45] Deformation potential theory was used to obtain approximate relaxation times for the 18 perovskite systems of interest as detailed in eqs 7 and 8, carried out in an identical manner to our previous work.[46,47] Here the index i corresponds to the charge carrier type and e and h to electrons and holes, respectively. C^{2D} represents the in-plane stiffness constant, and E_{VBM}, E_{CBM} are deformation potentials at the valence and conduction band edge, respectively, for which more information regarding the computational details can be found in the Computational Methods. The constants e, h_b, T represent the charge of an electron, Boltzmann constant, and temperature, respectively. Finally, μ_i represents the mobility of charge carriers of type i, and m_i^* represents the effective mass computed from parabolic fits of the valence and conduction bands of the SOC band structure.

$$\mu_i = \frac{2e\hbar^3 C^{2D}}{3k_b T E_i^2 m_i^*} \tag{7}$$

$$\tau_i = \frac{\mu_i m_i^*}{e} \tag{8}$$

The summarized findings regarding the elastic and thermoelectric properties of the 2DDPKs used in this study can be found in Table 2. The key quantity with which we quantify thermoelectric performance is the thermoelectric power factor (TPF) of holes and electrons at ambient and high temperatures of 300 and 800 K. The TPFs are computed as $TPF_{Ti} = S_{Ti}^2\sigma_{Ti}$ where S_{Ti} represents the Seebeck coefficient, σ_{Ti} the electrical conductivity, and the indices T and i again represent temperature and either electrons or holes as charge carriers. Figures S31−S47 show plots of S, σ, and TPF for electrons and holes ranging between 300 and 800 K for all 18 2DDPKs used in the present study. We note the flat bands associated with the frontier Au(d)-bands result in large effective masses, small electrical conductivities, and thereby extremely small TPFs, further reinforcing the notion that these Au-based 2DDPKs are unsuitable to not only photovoltaic but also thermoelectric applications. There is a consistent increase in TPFs when considering iodide as the halogen instead of chloride, with two representative examples in Figure 5a−d. This can be directly attributed to the fact that most band edges consist in part of the halogen p-orbitals, for which the dispersion of I(p) orbitals is more pronounced than that of Cl(p), resulting in favorable TE properties as they enter the BTEs through their band derivatives. Similarly, 2DDPKs which have strong dispersion at the band edge, such as those containing bismuth and antimony, show significantly improved

https://doi.org/10.1021/acsaem.3c03276
ACS Appl. Energy Mater. XXXX, XXX, XXX−XXX

TPFs when compared the narrower bands present in the only In- and Tl-containing 2DDPKs. This highlights the difficulty of obtaining an abundance of near-band gap transitions (such as is the case in the $In_{2S}Tl_{7S}Cl$ 2DDPK), while also obtaining optimal TE performance, as strong dispersion necessitates large fluctuations from the band gap across the BZ. With that said, the iodide based Bi- and Sb-containing 2DDPKs display promise for both n-doped and p-doped configurations, with TPF for p-doped configurations as high as 3.71 mW K^{-2} m^{-1} in InBiI, and n-doped configurations as high as 4.01 mW K^{-2} m^{-1} in InSbI at 300 K as seen in Figure 5a, b. This makes the InSbI 2DDPK one of the key candidates for implementation in hybrid PV-TE devices owing to its high TPF, which is maintained over a broad range of temperatures (Figure 5a) for both n- and p-doped configurations as well as a suitable 0.74 eV band gap.

CONCLUSION

In conclusion, we have conducted a systematic analysis of the structural, electronic, and thermoelectric properties of 18 2DDPKs consisting of a broad range of building components. Our analyses indicate the strong link between octahedral distortions and the electronegativity difference between the B-X and B′-X building components. Furthermore, we provide the simple linear relationship between band gaps in perovskite systems computed at the PBE level and the GLLB-sc level for direct comparison with experimental band gaps of $\tilde{E}_{GLLB-sc} = 1.59E_{PBE} + 0.17$ which can greatly aid in the future high-throughput screening of 2DDPKs. Additionally, we have identified several candidate photovoltaic materials, one of which is the mixed-oxidation state $In_{2S}Tl_{7S}Cl$ 2DDPK. This perovskite has optically active transitions as low as 1.41 eV across much of the BZ which is very close to the ideal band gap obtained in the Shockley-Quiesser limit for single junction solar cells of 1.34 eV. We have demonstrated how the novel approach of mixed-oxidation state cations in the 2DDPKs can alleviate concerns associated with otherwise parity forbidden transitions in DPKs which prevent utilization of an otherwise desirable material for photovoltaic applications. Finally, we highlight the InSbI-based 2DDPK for its potential in mixed PV-TE applications owing to the high TPF for both n-doped and p-doped configurations over a broad range of temperatures, as well as its strongly optically active direct bandgap of 0.74 eV. The combination of these insights can be used to guide the future generation of 2DDPK systems which are of interest for photovoltaic applications while mitigating structural and electronic concerns that are so commonly found in this class of materials.

COMPUTATIONAL METHODS

All density functional theory calculations were carried out using the plane-wave mode of the GPAW package with a kinetic energy cutoff of 550 eV.[48,49] A 4 × 4 × 2 k-point mesh was used for all variable and fixed cell optimizations, which were carried out until force components did not exceed 0.02 eV/Angstrom, and a 6 × 6 × 2 k-point mesh was used for self-consistent field calculations prior to non-self-consistent field calculations for the density of states and band structures. Self-consistent field calculations were converged to within 0.5 meV/valence electron and 10^{-4} e/valence electron for the energy and density, respectively. The atomic simulation environment, pymatgen, matminer, and Pyrovskite were used for the computation of structural descriptors of the optimized 2DDPK systems.[33,50−52] The PBE exchange correlation functional together was used in all calculations, and the DFT-D3 empirical dispersion correction was included to aid in accurately describing noncovalent interactions associated with the spacer molecules.[53,54] Band structures were computed with 100 k-points along the high symmetry paths, and unoccupied bands were converged up to 2 eV above the CBM.

For the computation of thermoelectric properties, we compute the effective masses and relaxation times as described in the manuscript. All thermoelectric properties are computed at fixed charge carrier densities of $\pm 10^{19}$ e/cm^3 for holes and electrons, respectively. To compute the deformation potentials E_{VBM} and E_{CBM}, we apply a linear fit to the energies at the band edges of the perovskite systems under the application of between −1.5% and 1.5% strain. We use the same −1.5% to 1.5% strain for computation of the in-plane stiffness constant C^{2D}, where we extract the second order coefficient of a parabolic fit. A relaxed-ion approach was used in all cases, as we find the clamped-ion approach to overestimate material stiffness.[55] Effective masses were computed using the effmass code with a 5-point least-squares fit, and all effective masses were computed from the SOC included band structures, as SOC provides more reliable curvature at the band edge.[56]

ASSOCIATED CONTENT

Supporting Information

The Supporting Information is available free of charge at https://pubs.acs.org/doi/10.1021/acsaem.3c03276.

Additional details regarding structural and electronic properties about the perovskites utilized in this work; schematic representation of perovskite systems under investigation; plots of electronic band structure, density of states, and bond distance distributions of 2DDPKs under investigation; plots demonstrating thermoelectric performance of the 2DDPKs under investigation (PDF)

AUTHOR INFORMATION

Corresponding Author

Dhara J. Trivedi − *Department of Physics, Clarkson University, Potsdam, New York 13699, United States;* orcid.org/0000-0002-8151-3929; Email: dtrivedi@clarkson.edu

Author

Robert Stanton − *Department of Physics, Clarkson University, Potsdam, New York 13699, United States;* orcid.org/0000-0002-4989-6958

Complete contact information is available at: https://pubs.acs.org/10.1021/acsaem.3c03276

Notes

The authors declare no competing financial interest.

ACKNOWLEDGMENTS

The authors gratefully acknowledge support from the U.S. National Science Foundation (ECCS-2138728). This work used Bridges-2 at Pittsburgh Supercomputing Center through allocation CHE210004 from the Advanced Cyberinfrastructure Coordination Ecosystem: Services & Support (ACCESS) program, which is supported by National Science Foundation grants #2138259, #2138286, #2138307, #2137603, and #2138296.

REFERENCES

(1) Karna, L. R.; Upadhyay, R.; Ghosh, A. All-Inorganic Perovskite Photovoltaics for Power Conversion Efficiency of 31%. *Sci. Rep* **2023**, *13* (1), 15212.

(2) Min, H.; Lee, D. Y.; Kim, J.; Kim, G.; Lee, K. S.; Kim, J.; Paik, M. J.; Kim, Y. K.; Kim, K. S.; Kim, M. G.; Shin, T. J.; Il Seok, S. Perovskite Solar Cells with Atomically Coherent Interlayers on SnO2 Electrodes. *Nature* **2021**, *598* (7881), 444−450.
(3) Wu, M.; Shi, J.; Zhang, M.; Cen, Y.; Guo, W.; Zhu, Y. Promising Photovoltaic and Solid-State-Lighting Materials: Two-Dimensional Ruddlesden-Popper Type Lead-Free Halide Double Perovskites $Cs_{n+1}In_{n/2}Sb_{n/2}I_{3n+1}$ (n = 3) and $Cs_{n+1}In_{n/2}Sb_{n/2}Cl_{3n+1}/Cs_{m+1}Cu_{m/2}Bi_{m/2}Cl_{3m+1}$ (n = 3, m = 1). *J. Mater. Chem. C* **2018**, *6* (43), 11575−11586.
(4) Chen, S.; Deng, Y.; Xiao, X.; Xu, S.; Rudd, P. N.; Huang, J. Preventing Lead Leakage with Built-in Resin Layers for Sustainable Perovskite Solar Cells. *Nat. Sustain* **2021**, *4* (7), 636−643.
(5) Zhang, H.; Li, K.; Sun, M.; Wang, F.; Wang, H.; Jen, A. K. Y. Design of Superhydrophobic Surfaces for Stable Perovskite Solar Cells with Reducing Lead Leakage. *Adv. Energy Mater.* **2021**, *11* (41), 2102281.
(6) Jin, S. Can We Find the Perfect A-Cations for Halide Perovskites? *ACS Energy Lett.* **2021**, *6* (9), 3386−3389.
(7) Gélvez-Rueda, M. C.; Cao, D. H.; Patwardhan, S.; Renaud, N.; Stoumpos, C. C.; Schatz, G. C.; Hupp, J. T.; Farha, O. K.; Savenije, T. J.; Kanatzidis, M. G.; Grozema, F. C. Effect of Cation Rotation on Charge Dynamics in Hybrid Lead Halide Perovskites. *J. Phys. Chem. C* **2016**, *120* (30), 16577−16585.
(8) Metrangolo, P.; Canil, L.; Abate, A.; Terraneo, G.; Cavallo, G. Halogen Bonding in Perovskite Solar Cells: A New Tool for Improving Solar Energy Conversion. *Angew. Chem. Int. Ed* **2022**, *61* (11), e202114793.
(9) Bi, L.-Y.; Hu, Y.-Q.; Li, M.-Q.; Hu, T.-L.; Zhang, H.-L.; Yin, X.-T.; Que, W.-X.; Lassoued, M. S.; Zheng, Y.-Z. Two-Dimensional Lead-Free Iodide-Based Hybrid Double Perovskites: Crystal Growth, Thin-Film Preparation and Photocurrent Responses. *Journal of Materials Chemistry A* **2019**, *7* (34), 19662−19667.
(10) Wu, M.; Shi, J.; Zhang, M.; Cen, Y.; Guo, W.; Zhu, Y. Promising Photovoltaic and Solid-State-Lighting Materials: Two-Dimensional Ruddlesden-Popper Type Lead-Free Halide Double Perovskites $Cs_{n+1}In_{n/2}Sb_{n/2}I_{3n+1}$ (n = 3) and $Cs_{n+1}In_{n/2}Sb_{n/2}Cl_{3n+1}/Cs_{m+1}Cu_{m/2}Bi_{m/2}Cl_{3m+1}$ (n = 3, m = 1). *J. Mater. Chem. C* **2018**, *6* (43), 11575−11586.
(11) Kung, P.-K.; Li, M.-H.; Lin, P.-Y.; Jhang, J.-Y.; Pantaler, M.; Lupascu, D. C.; Grancini, G.; Chen, P. Lead free Double Perovskites for Perovskite Solar Cells. *Solar RRL* **2020**, *4* (2), 1900306.
(12) Krishna, A.; Gottis, S.; Nazeeruddin, M. K.; Sauvage, F. Mixed Dimensional 2D/3D Hybrid Perovskite Absorbers: The Future of Perovskite Solar Cells? *Adv. Funct. Mater.* **2019**, *29* (8), 1806482.
(13) Kopacic, I.; Friesenbichler, B.; Hoefler, S. F.; Kunert, B.; Plank, H.; Rath, T.; Trimmel, G. Enhanced Performance of Germanium Halide Perovskite Solar Cells through Compositional Engineering. *ACS Applied Energy Materials* **2018**, *1* (2), 343−347.
(14) Chen, M.; Shan, Z.; Dong, X.; Liu, S. F.; Xu, Z. Discovering Layered Lead-Free Perovskite Solar Absorbers via Cation Transmutation. *Nanoscale Horizons* **2023**, *8* (4), 483−488.
(15) Fu, P.; Liu, Y.; Yu, S.; Yin, H.; Yang, B.; Ahmad, S.; Guo, X.; Li, C. Dion-Jacobson and Ruddlesden-Popper Double-Phase 2D Perovskites for Solar Cells. *Nano Energy* **2021**, *88*, 106249.
(16) Stanton, R.; Trivedi, D. J. Charge Carrier Dynamics at the Interface of 2D Metal-Organic Frameworks and Hybrid Perovskites for Solar Energy Harvesting. *Nano Lett.* **2023**, *23* (24), 11932−11939.
(17) Kim, C.; Huan, T. D.; Krishnan, S.; Ramprasad, R. A Hybrid Organic-Inorganic Perovskite Dataset. *Sci. Data* **2017**, *4* (1), 170057.
(18) Marchenko, E. I.; Fateev, S. A.; Petrov, A. A.; Korolev, V. V.; Mitrofanov, A.; Petrov, A. V.; Goodilin, E. A.; Tarasov, A. B. Database of Two-Dimensional Hybrid Perovskite Materials: Open-Access Collection of Crystal Structures, Band Gaps, and Atomic Partial Charges Predicted by Machine Learning. *Chem. Mater.* **2020**, *32* (17), 7383−7388.
(19) Yılmaz, B.; Odabaşı, Ç.; Yıldırım, R. Efficiency and Stability Analysis of 2D/3D Perovskite Solar Cells Using Machine Learning. *Energy Technology* **2022**, *10* (3), 2100948.
(20) Zhou, J.; Xie, P.; Wang, C.; Bian, T.; Chen, J.; Liu, Y.; Guo, Z.; Chen, C.; Pan, X.; Luo, M.; et al. Hybrid Double Perovskite Derived Halides Based on Bi and Alkali Metals (K, Rb): Diverse Structures, Tunable Optical Properties and Second Harmonic Generation Responses. *Angew. Chem., Int. Ed.* **2023**, *62* (35), e202307646.
(21) Vargas, B.; Rodrıguez-López, G.; Solis-Ibarra, D. The Emergence of Halide Layered Double Perovskites. *ACS Energy Letters* **2020**, *5* (11), 3591−3608.
(22) Blancon, J.-C.; Even, J.; Stoumpos, C. C.; Kanatzidis, M. G.; Mohite, A. D. Semiconductor Physics of Organic-Inorganic 2D Halide Perovskites. *Nature Nanotechnol.* **2020**, *15* (12), 969−985.
(23) Meng, W.; Wang, X.; Xiao, Z.; Wang, J.; Mitzi, D. B.; Yan, Y. Parity-Forbidden Transitions and Their Impact on the Optical Absorption Properties of Lead-Free Metal Halide Perovskites and Double Perovskites. *J. Phys. Chem. Lett.* **2017**, *8* (13), 2999−3007.
(24) Luo, J.; Li, S.; Wu, H.; Zhou, Y.; Li, Y.; Liu, J.; Li, J.; Li, K.; Yi, F.; Niu, G.; Tang, J. Cs2AgInCl6 Double Perovskite Single Crystals: Parity Forbidden Transitions and Their Application for Sensitive and Fast UV Photodetectors. *Acs Photonics* **2018**, *5* (2), 398−405.
(25) Appadurai, T.; Kashikar, R.; Sikarwar, P.; Antharjanam, S.; Nanda, B. R. K.; Chandiran, A. K. Manipulation of Parity and Polarization through Structural Distortion in Light-Emitting Halide Double Perovskites. *Commun. Mater.* **2021**, *2* (1), 68.
(26) Tian, X.; Zhang, Y.; Zheng, R.; Wei, D.; Liu, J. Two-Dimensional Organic-Inorganic Hybrid Ruddlesden-Popper Perovskite Materials: Preparation, Enhanced Stability, and Applications in Photodetection. *Sustainable Energy & Fuels* **2020**, *4* (5), 2087−2113.
(27) Li, Y.; Yang, T.; Xu, Z.; Liu, X.; Huang, X.; Han, S.; Liu, Y.; Li, M.; Luo, J.; Sun, Z. Dimensional Reduction of Cs2AgBiBr6: A 2D Hybrid Double Perovskite with Strong Polarization Sensitivity. *Angew. Chem., Int. Ed.* **2020**, *59* (9), 3429−3433.
(28) Singh, A.; Yuan, B.; Rahman, M. H.; Yang, H.; De, A.; Park, J. Y.; Zhang, S.; Huang, L.; Mannodi-Kanakkithodi, A.; Pennycook, T. J.; Dou, L. Two-Dimensional Halide Pb-Perovskite-Double Perovskite Epitaxial Heterostructures. *J. Am. Chem. Soc.* **2023**, *145* (36), 19885−19893.
(29) Zhang, Z.; Jiang, Y.; Dong, Z.; Chu, Y.; Xu, J. 2D/2D Inorganic/Organic Hybrid of Lead-Free Cs2AgBiBr6 Double Perovskite/Covalent Triazine Frameworks with Boosted Charge Separation and Efficient CO2 Photoreduction. *Inorg. Chem.* **2022**, *61* (40), 16028−16037.
(30) Fu, D.; Wu, S.; Liu, Y.; Yao, Y.; He, Y.; Zhang, X.-M. A Lead-Free Layered Dion-Jacobson Hybrid Double Perovskite Constructed by an Aromatic Diammonium Cation. *Inorganic Chemistry Frontiers* **2021**, *8* (14), 3576−3580.
(31) Smith, M. D.; Connor, B. A.; Karunadasa, H. I. Tuning the Luminescence of Layered Halide Perovskites. *Chem. Rev.* **2019**, *119* (5), 3104−3139.
(32) Kuisma, M.; Ojanen, J.; Enkovaara, J.; Rantala, T. T. Kohn-Sham Potential with Discontinuity for Band Gap Materials. *Phys. Rev. B* **2010**, *82* (11), 115106.
(33) Stanton, R.; Trivedi, D. J. Pyrovskite: A Software Package for the High-Throughput Construction, Analysis, and Featurization of Two- and Three-Dimensional Perovskite Systems. *J. Chem. Phys.* **2023**, *159* (6), 064803.
(34) Zhang, L.; Luo, J.; Liu, B.; Yang, J.; Cai, M.-Q. Effect of Substituting on the Transition Dipole Moment of the Double Perovskite Cs2AgInCl6. *J. Phys.: Condens. Matter* **2024**, *36* (7), 075703.
(35) Kibbou, M.; Haman, Z.; Khossossi, N.; Singh, D.; Essaoudi, I.; Ainane, A.; Ahuja, R. Probing the Electronic, Optical and Transport Properties of Halide Double Perovskites Rb2InSb (Cl, Br) 6 for Solar Cells and Thermoelectric Applications. *J. Solid State Chem.* **2022**, *312*, 123262.
(36) Ou, T.; Zhuang, Q.; Yan, H.; Feng, S.; Li, P.; Ma, X. Lead-Free Halide Double Perovskites Rb2InSbX6 (X = F, Cl, Br, I): A First-Principles Study of Structural and Optoelectrical Properties. *Chem. Phys.* **2023**, *573*, 112015.

https://doi.org/10.1021/acsaem.3c03276
ACS Appl. Energy Mater. XXXX, XXX, XXX−XXX

(37) Bourgault, D.; Martin, C.; Michel, C.; Hervieu, M.; Raveau, B. Thallium Mixed Valence-Tl (I)/Tl (III) in "2212" Thallium Cuprates: The Oxides TlIII2-(X3) TlI1- xBa1+ xLnCu2O8. *Physica C: Superconductivity and its Applications* **1989**, *158* (3), 511−518.
(38) Shannon, R. t; Prewitt, C. Revised Values of Effective Ionic Radii. *Acta Crystallographica Section B: Structural Crystallography and Crystal Chemistry* **1970**, *26* (7), 1046−1048.
(39) Goldschmidt, V. M. Die Gesetze Der Krystallochemie. *Naturwissenschaften* **1926**, *14* (21), 477−485.
(40) Li, C.; Lu, X.; Ding, W.; Feng, L.; Gao, Y.; Guo, Z. Formability of Abx3 (X = f, Cl, Br, i) Halide Perovskites. *Acta Crystallographica Section B: Structural Science* **2008**, *64* (6), 702−707.
(41) Zhan, X.; Chen, X.; Li, C.; Jin, T.; Wang, Y.; Chen, Z.-N.; Wu, T.; Chen, J.; Zhuang, W. Can Lead-Free Double Halide Perovskites Serve as Proper Photovoltaic Absorber? *J. Phys. Chem. Lett.* **2023**, *14* (48), 10784−10793.
(42) Jesper Jacobsson, T.; Correa-Baena, J.-P.; Pazoki, M.; Saliba, M.; Schenk, K.; Gratzel, M.; Hagfeldt, A. Exploration of the Compositional Space for Mixed Lead Halogen Perovskites for High Efficiency Solar Cells. *Energy Environ. Sci.* **2016**, *9* (5), 1706−1724.
(43) Tran, F.; Doumont, J.; Kalantari, L.; Blaha, P.; Rauch, T.; Borlido, P.; Botti, S.; Marques, M. A. L.; Patra, A.; Jana, S.; Samal, P. Bandgap of Two-Dimensional Materials: Thorough Assessment of Modern Exchange-Correlation Functionals. *J. Chem. Phys.* **2021**, *155* (10), 104103.
(44) Pandey, M.; Jacobsen, K. W.; Thygesen, K. S. Band Gap Tuning and Defect Tolerance of Atomically Thin Two-Dimensional Organic-Inorganic Halide Perovskites. *J. Phys. Chem. Lett.* **2016**, *7* (21), 4346−4352.
(45) Madsen, G. K.; Carrete, J.; Verstraete, M. J. BoltzTraP2, a Program for Interpolating Band Structures and Calculating Semi-Classical Transport Coefficients. *Comput. Phys. Commun.* **2018**, *231*, 140−145.
(46) Stanton, R.; Gupta, S. K.; Trivedi, D. J. Probing Strain-Induced Effects on Performance of Low-Dimensional Hybrid Perovskites for Solar Energy Harvesting. *ACS Appl. Mater. Interfaces* **2022**, *14* (30), 34603−34611.
(47) Stanton, R.; Trivedi, D. J. Atomistic Description of the Impact of Spacer Selection on Two-Dimensional (2D) Perovskites: A Case Study of 2D Ruddlesden-Popper CsPbI3 Analogues. *J. Phys. Chem. Lett.* **2022**, *13* (51), 12090−12098.
(48) Mortensen, J. J.; Larsen, A. H.; Kuisma, M.; Ivanov, A. V.; Taghizadeh, A.; Peterson, A.; Haldar, A.; Dohn, A. O.; Schäfer, C.; Jónsson, E. Ö. GPAW: Open Python Package for Electronic-Structure Calculations. *arXiv Preprint*, 2023,arXiv:2310.14776.
(49) Mortensen, J. J.; Hansen, L. B.; Jacobsen, K. W. Real-Space Grid Implementation of the Projector Augmented Wave Method. *Phys. Rev. B* **2005**, *71* (3), 035109.
(50) Hjorth Larsen, A.; Jørgen Mortensen, J.; Blomqvist, J.; Castelli, I. E; Christensen, R.; Dułak, M.; Friis, J.; Groves, M. N; Hammer, B.ør.; Hargus, C.; et al. The Atomic Simulation Environment—a Python Library for Working with Atoms. *J. Phys.: Condens. Matter* **2017**, *29* (27), 273002.
(51) Ong, S. P.; Richards, W. D.; Jain, A.; Hautier, G.; Kocher, M.; Cholia, S.; Gunter, D.; Chevrier, V. L.; Persson, K. A.; Ceder, G. Python Materials Genomics (Pymatgen): A Robust, Open-Source Python Library for Materials Analysis. *Comput. Mater. Sci.* **2013**, *68*, 314−319.
(52) Ward, L.; Dunn, A.; Faghaninia, A.; Zimmermann, N. E.; Bajaj, S.; Wang, Q.; Montoya, J.; Chen, J.; Bystrom, K.; Dylla, M.; et al. Matminer: An Open Source Toolkit for Materials Data Mining. *Comput. Mater. Sci.* **2018**, *152*, 60−69.
(53) Perdew, J. P.; Burke, K.; Ernzerhof, M. Generalized Gradient Approximation Made Simple. *Physical review letters* **1996**, *77* (18), 3865.
(54) Grimme, S.; Antony, J.; Ehrlich, S.; Krieg, H. A Consistent and Accurate Ab Initio Parametrization of Density Functional Dispersion Correction (DFT-D) for the 94 Elements H-Pu. *J. Chem. Phys.* **2010**, *132* (15), 154104.
(55) Fei, R.; Li, W.; Li, J.; Yang, L. Giant Piezoelectricity of Monolayer Group IV Monochalcogenides: SnSe, SnS, GeSe, and GeS. *Appl. Phys. Lett.* 2015, *107* (17).
(56) Whalley, L. D. Effmass: An Effective Mass Package. *Journal of Open Source Software* **2018**, *3* (28), 797.

https://doi.org/10.1021/acsaem.3c03276
ACS Appl. Energy Mater. XXXX, XXX, XXX−XXX